

Coulomb-explosion imaging using a pixel-imaging mass-spectrometry cameraCraig S. Slater, Sophie Blake, Mark Brouard,^{*} and Alexandra Lauer*The Physical and Theoretical Chemistry Laboratory, Department of Chemistry, University of Oxford, South Parks Road, Oxford OX1 3QZ, United Kingdom*

Claire Vallance

Chemistry Research Laboratory, Department of Chemistry, University of Oxford, Mansfield Road, Oxford OX1 3TA, United Kingdom

C. Sean Bohun

*Faculty of Science, University of Ontario Institute of Technology, 2000 Simcoe Street, North Oshawa, Ontario, Canada L1K 2E8*Lauge Christensen and Jens H. Nielsen[†]*Department of Physics and Astronomy, Aarhus University, DK-8000 Aarhus C, Denmark*

Mikael P. Johansson

*Laboratory for Instruction in Swedish, Department of Chemistry, University of Helsinki, A. I. Virtanens plats 1, P.O. Box 55, FI-00014, Helsinki, Finland*Henrik Stapelfeldt[‡]*Department of Chemistry and Interdisciplinary Nanoscience Center, Aarhus University, DK-8000 Aarhus C, Denmark*

(Received 25 March 2015; published 28 May 2015)

Femtosecond laser-induced Coulomb-explosion imaging of 3,5-dibromo-3',5'-difluoro-4'-cyanobiphenyl molecules prealigned in space is explored using a pixel-imaging mass-spectrometry (PIImS) camera. The fast-event-triggered camera allows the concurrent detection of the correlated two-dimensional momentum images, or covariance maps, of all the ionic fragments resulting from fragmentation of multiple molecules in each acquisition cycle. Detailed simulation of the covariance maps reveals that they provide rich information about the parent molecular structure and fragmentation dynamics. Future opportunities for imaging the real-time dynamics of intramolecular processes are considered.

DOI: [10.1103/PhysRevA.91.053424](https://doi.org/10.1103/PhysRevA.91.053424)

PACS number(s): 33.80.Gj, 33.15.Hp, 33.80.Rv, 34.50.Gb

I. INTRODUCTION

The field of femtochemistry has advanced rapidly over recent years and has revolutionized the study of molecular dynamics. A tantalizing prospect is that of the “molecular movie,” in which the detailed structure of a chemical system is recorded as a reaction or some other process unfolds. However, achieving this level of insight is not without its challenges. It is a difficult undertaking to perform such measurements without significantly perturbing the structure of the target system as a direct result of performing the measurement itself. Furthermore, determining the structure of a molecular system, with three coordinates describing the position of each atom, requires a substantial amount of experimental information.

Coulomb-explosion imaging (CEI) using tabletop visible or near-IR femtosecond laser systems in the visible or near-IR provides molecular structural information on an ultrafast time scale [1–3]. The characteristic structural coordinates of a molecular system are inferred through the investigation of the rapid fragmentation dynamics of the highly charged molecular

ion, termed a Coulomb explosion. The molecular ion is generated by the swift removal of several electrons following irradiation by a short, intense laser pulse supplied from a tabletop femtosecond laser system [4]. The forces governing the subsequent process of molecular ion dissociation are primarily Coulombic in nature, and the dissociation dynamics may be described, to a good approximation, using classical laws of motion in a Coulomb potential.

So far, investigations of the usefulness of CEI as an effective probe of molecular structure have largely been confined to diatomic, triatomic, or small polyatomic systems, such as H₂ [5], SO₂ [6], and substituted methyl derivatives [7,8]. Building on our previous work [3,9], the experimental data and ion-trajectory simulations reported in this paper explore the potential of CEI for determining elements of molecular structure of moderately large polyatomic systems, using a substituted biphenyl molecule (relative molecular mass, RMM = 373) as an example of such a target. The study also highlights interesting dynamical features of the Coulomb explosion itself.

The conventional means of determining the configuration and absolute structure of a molecule following Coulomb explosion depends on the concurrent measurement of the full three-dimensional (3D) momenta of all fragment ions following molecular fragmentation using a multiparticle 3D-imaging detector [10–13]. The relationships between these 3D momenta are determined through a coincidence analysis, thereby allowing inferences to be made on the parent molecular

^{*}mark.brouard@chem.ox.ac.uk[†]Present address: Research Software Development Group, Research IT Services, University College London, Podium Building (1st Floor), Gower Street, London WC1E 6BT, United Kingdom.[‡]henriks@chem.au.dk

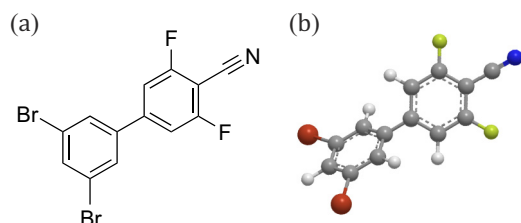


FIG. 1. (Color online) (a) Skeleton and (b) ball and stick representations of the 3,5-dibromo-3',5'-difluoro-4'-cyanobiphenyl (DBrDFCNBph) molecule.

structure. However, due to the large number of fragment ions that are necessarily produced following Coulomb explosion of extended molecular structures and the correspondingly congested time-of-flight spectrum that results, alternative strategies to 3D momentum imaging are investigated based on a statistical correlation of two-dimensional (2D) fragment-ion momenta in experiments employing spatially prealignment target molecules [3,14]. The unique capabilities of a pixel-imaging mass-spectrometry (PImMS) camera [15,16] when combined with a velocity-map [17] ion-imaging [18] (VMI) spectrometer are central to the work described in this paper.

This paper is structured as follows. In Sec. II we describe the experimental procedures employed and give a brief summary of the specific feature of the PImMS camera used in this work. The main results and discussion are contained in Sec. III, which presents the experimental results, outlines the covariance analysis employed to convert the raw ion-imaging data into covariance maps, and describes and presents the details of classical simulations of the Coulomb explosion dynamics and the covariance image data. Finally, Sec. IV briefly summarizes the key findings and outlines potential directions for future study.

II. EXPERIMENT

A. Overview

The target molecule used in this study was 3,5-dibromo-3',5'-difluoro-4'-cyanobiphenyl ($C_{13}H_5F_2Br_2N$, DBrDFCNBph), the structure of which is shown in Fig. 1. DBrDFCNBph is not commercially available and was synthesized specifically for these experiments following the procedure described in the appendix of Ref. [3]. The molecules possess a stereogenic axis that lies along the C-C bond between the two phenyl rings, which is also the C_2 symmetry axis. The C_2 symmetry axis also coincides with the most polarizable axis (MPA) of the molecule, as discussed further below. Internal hindered rotation about this axis takes place on a torsional potential-energy surface, which has two equal minima when the angle between the rings is $\pm 39^\circ$ [3]. The two conformers that result from localization of the structure around these minima are the R_a ($+39^\circ$) and S_a (-39°) enantiomers. At room temperature, the molecules have sufficient energy to overcome the potential barrier between the two enantiomeric conformers (calculated to be around 550 cm^{-1} [19]), resulting in essentially unhindered rotation of the phenyl rings about the

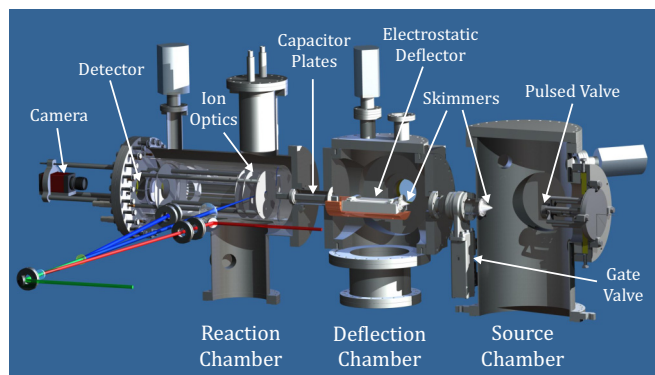


FIG. 2. (Color online) The Aarhus VMI spectrometer used in the current experiments. The principal components are identified and labeled; see text for details.

central C-C bond. However, at the low temperatures achieved through the supersonic expansion of the gaseous sample into the vacuum chamber ($\sim 1\text{ K}$), the molecules are effectively frozen into one of the two enantiomeric forms.

The experimental apparatus has been described in detail previously [3]. A schematic is shown in Fig. 2. Briefly, from right to left, the molecular beam is introduced into the source chamber by way of a supersonic expansion through a high-pressure Even-Lavie pulsed valve [20], after which it is skimmed twice in order to collimate the expansion. The molecular beam then travels through a 15-cm-long electrostatic deflector, which acts to separate the molecules with respect to their rotational quantum states and, by selection of the rotationally coldest part of the molecular beam, thereby improves the degree of adiabatic alignment achievable using the nanosecond laser pulse [21]. The molecular beam then passes into the reaction chamber, which contains the ion optics assembly and the field-free drift region. The ion optics are composed of three open electrodes, which act as an electrostatic lens, with the applied high voltages optimized to effect velocity-map [17] imaging of the ions onto the detector. The laser pulses enter the experiment through a fused silica window on one side of the reaction chamber, intersecting the molecular beam in a perpendicular manner between the repeller and extractor electrodes of the ion optics assembly. Once formed, the ions are accelerated along the flight tube by the electric field of the ion optics and are focused onto a position-sensitive detector, comprising a pair of chevron-stacked MCPs coupled to a P47 phosphor screen. The individual ion events imaged on the phosphor screen are captured using a PImMS camera, which is described in more detail in Sec. II B.

The molecules are exposed to two distinct laser pulses while in the interaction region, hereafter referred to as the alignment and probe laser pulses. The alignment laser pulse is a linearly polarized 10-ns (FWHM) laser pulse from a Nd:YAG laser (1064 nm , $8 \times 10^{11}\text{ W/cm}^2$), which spatially aligns the MPA of the molecules in the laboratory frame (see further below). The intensity is carefully adjusted so as to minimize multiphoton dissociation or ionization. With

the YAG pulse polarization aligned perpendicular to the face of the detector (“perpendicular alignment”) the MPA, which coincides with the C_2 symmetry axis, is confined along this direction. Alternatively, with the YAG pulse polarized parallel to the detector face (“parallel alignment”) the molecules are imaged in side view. Note that with linearly polarized light, the C_2 symmetry axis of the molecule is one-dimensional (1D) aligned in the laboratory frame, but the molecule is free to rotate about this axis. A 3D alignment of the molecule is also possible using elliptically polarized radiation [3,14,19] but is not considered further here.

The probe laser pulse which induces Coulomb explosion is an intense 30-fs (FWHM) laser pulse (800 nm, 3×10^{14} W/cm²), which is overlapped with the alignment pulse in space and time, and is used to induce nonresonant multiphoton ionization and Coulomb explosion of the target molecules. Its polarization was linear and kept in the same direction as the YAG pulse polarization. The repetition rate of the experiment is limited by that of the nanosecond laser system to 20 Hz.

B. The PImMS camera

Ion events imaged on the phosphor screen were recorded using the PImMS camera [22–25]: a pixelated photon-sensitive event-counting sensor. The PImMS sensor comprises a 2D array of 72×72 pixels, each of which can store the time stamps of up to four events per acquisition cycle. When a sufficient number of photons are collected by a pixel, such that a predetermined threshold is exceeded, the value of an internal global time code signal is stored in one of the four memory registers of the pixel. The internal clock may be synchronized to an external trigger and runs at a frequency of up to 80 MHz, corresponding to a minimum time bin width of 12.5 ns. The data are read out from the pixel memories at the end of each acquisition cycle, providing the x and y coordinates of each event, along with the corresponding time codes and the acquisition cycle number. As a light-sensitive detector, the PImMS camera may be used as a direct replacement for the CCD or intensified CCD camera often used in conventional ion- or electron-imaging experiments [26,27].

The unique properties of the PImMS camera are crucial to the success of these measurements. There are alternative devices that are capable of recording ion events with the high degree of temporal and spatial accuracy [12,28–34] required in order to perform a correlation analysis between the various fragment ions. However, the unique ability of the PImMS camera to record a large number of ion events simultaneously is decisive in this application. The delay-line detector [12,28,29,31,32,34] is an alternative device which can provide very precise ion arrival-time information. Although there has been work done recently on three-layer delay-line detectors, which can detect many ions of the same mass in the same shot [34], standard delay-line detectors are generally constrained by the number of ions that may be detected concurrently. Such technology would be unsuitable for the recording of data following the Coulomb explosion of moderately large polyatomic systems containing a number of identical constituent atoms. Alternative silicon-based detectors, such as the TimePix/MediPix family [33], overcome this limitation, but at the expense of an imperfect and nonuniform collection

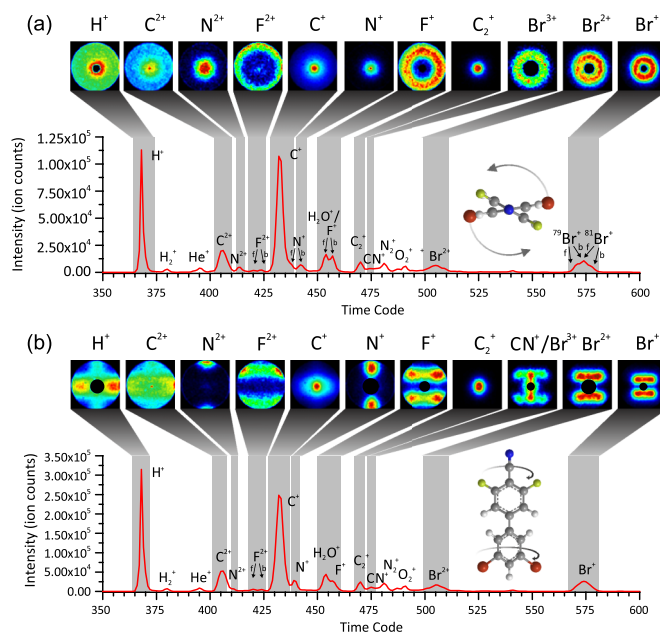


FIG. 3. (Color online) Time-of-flight spectra and examples of laboratory-frame images for (a) perpendicular and (b) parallel alignment of the molecules to the detector plane. The peaks are assigned, and images corresponding to a selection of fragment ions are shown above the time-of-flight spectrum. The gray shading identifies the range of time codes contributing to each image. Where appropriate, the forward- and backward-scattered peaks are identified by arrows labeled with *f* and *b*, respectively.

efficiency of late-arriving ions. This is a direct consequence of each pixel containing only a single memory register, resulting in shadowing of later mass peaks by those occurring at earlier times. When a large variety of product fragments are produced, spanning a large range of mass and charge states, this limitation has the potential to systematically reduce the fidelity of the experimental data. The PImMS sensor, on the other hand, has four memory registers for each individual pixel, allowing the detection of up to four events per pixel per acquisition cycle; an empty fourth register shows that no events have been missed. It should be noted that this issue has also been addressed by the latest version of TimePix, TimePix3 [35,36].

III. RESULTS AND DISCUSSION

A. Time-of-flight spectra

1. Time-of-flight spectra from PImMS data

The time-of-flight spectra following Coulomb explosion of DBRDFCNBph with the MPA aligned perpendicular and parallel to the detector plane, as recorded by the PImMS camera, are shown in Figs. 3(a) and 3(b), respectively. The data were recorded over 125 000 and 50 000 laser shots, respectively, and have been processed according to the centroiding scheme outlined in Ref. [9] in order to extract the most accurate timing information.

The majority of the important features are well resolved, and the additional velocity information provided by the spatial resolution of the detection system aids the assignment of the

peaks. In addition to the time-of-flight information, the overlapping ion signals often have significantly different velocity signatures, allowing their separation in the spatial domain. For example, the F^+ signal ($m/z = 19$) is almost coincident in the time domain with the signal from background water in the chamber ($m/z = 18$). However, since the Coulomb explosion process imparts a substantial velocity to the fragment ions, the F^+ signal is easily separated from that of H_2O^+ , which has almost zero velocity and impacts exclusively on the center of the detector. In several instances the contribution from background contaminants in the center of the image has been removed. In addition to signal assigned to the Coulomb explosion of DBrDFCNBph, the time-of-flight spectra contain a number of peaks resulting from the ionization of background gas in the target chamber, notably He^+ , H_2O^+ , N_2^+ , and O_2^+ .

While at first glance the time-of-flight spectra for the two different molecular alignments appear similar, a closer examination reveals interesting differences. Most pronounced is the different shape of the F^+ and Br^+ signals: in perpendicular alignment, these signals are split due to the contributions from ions scattered forward and backward along the time-of-flight axis. In the case of Br^+ , the approximately equal abundance of the $^{79}Br^+$ and $^{81}Br^+$ isotopes, coupled with the forward-backward peak for each isotope, leads to a triplet-shaped peak structure.

It appears from the time-of-flight spectra that the vast majority of fragments are atomic ions. If the YAG pulse is blocked, more molecular fragments, including small amounts of the parent molecular ion, are observed. The YAG pulse not only aligns the molecules but also causes further ionization and fragmentation of the molecular ions created by the probe pulse. We believe the ionization and fragmentation result from absorption of one or more YAG photons by the molecular ions shortly after the probe pulse. Despite the contribution of this postprobe pulse process to the ions recorded, we show in the following sections that the ion images, and, notably, the covariance images, are dominated by ions with a strong velocity correlation. For this correlation to be preserved, secondary ionization and fragmentation caused by YAG photons must happen on the same short time scale as direct Coulomb explosion, allowing the extraction of extensive structural information about the neutral parent molecule as well as about the Coulomb fragmentation dynamics.

2. Ion yields

Further insight into the mechanism of Coulomb explosion may be gained through an assessment of the relative yields of the various ionic photofragments, as presented in Table I. The values in Table I have been calculated from the integrals of the peaks in the time-of-flight spectrum, following Coulomb explosion of perpendicularly aligned target molecules. Since the atomic ions dominate the spectrum, only these have been considered in the ion yield calculations. The relative yields of the ions have been grouped according to the neutral parent and normalized such that the yield of H^+ ions is equal to 5, which corresponds to the stoichiometry of the parent molecule. The ion yields have been determined without making allowance of the variation in MCP detection efficiency with ion mass, which will favor the detection of the lighter ions. We believe that the

TABLE I. Tabulated values of the ion intensities, as measured from the integrals of the peaks in the time-of-flight spectrum recorded following Coulomb explosion of perpendicularly aligned molecules from the time-of-flight spectrum presented in Fig. 3(a). The cumulative ionization energies (IE) are listed as an approximate guide to the energetics of production of each species. The estimated ion yields assume uniform MCP detection efficiency with ion mass.

Parent atom	Ion	Cumulative IE (eV)	Intensity (ion counts)	Relative intensity	Relative charge per atom
H	H^+	13.6	195364	5.0	1.0
C	C^+	11.26	406006	12.78	0.98
	C^{2+}	35.64	93425		
N	N^+	14.53	527401	2.09	2.09
	N^{2+}	44.13	290861		
F	F^+	17.42	93766	2.70	1.35
	F^{2+}	52.39	11751		
Br	Br^+	11.81	77973	3.82	1.91
	Br^{2+}	33.4	51222		
	Br^{3+}	68.4	20168		

qualitative conclusions below are unlikely to be altered by not allowing for the different detection efficiencies.

From the data presented in Table I, it is clear that the relative ion yields differ somewhat from those expected based on purely stoichiometric arguments. The yield of the fluorine and bromine fragment ions is substantially higher than the value of 2 expected on the basis of stoichiometry, with observed yields of 2.70 and 3.82, respectively. The higher relative yield of bromine ions may be attributed to the much lower ionization energy of bromine compared to fluorine and the reduced collection efficiency of fluorine ions due to the limited size of the detector. However, the increased yield of fluorine ions relative to hydrogen and carbon ions is interesting, given the highly electronegative character of the atoms. The most pronounced enhancement in ion yield when compared to the stoichiometric ratios of the parent molecule is found for the nitrogen fragment ions, for which the ion yield is more than double that expected. The same trend is seen when the relative charges attributed to each substituent are calculated from the experimental ion yields. These are determined by dividing the observed ion yields by the number of like atoms in the molecule. By inference, as seen from Table I, the charge carried by ions corresponding to the peripheral N, F, and Br substituents is substantially higher than that calculated for the carbon skeleton.

The ion yields suggest significant ionization and fragmentation into atomic ions and reflect the detailed Coulomb explosion dynamics.

3. Time-of-flight covariance

Acquisition of event-based data using the PImMS camera allows the measurement of the correlation between the various mass peaks through a covariance analysis of the data [37–39].

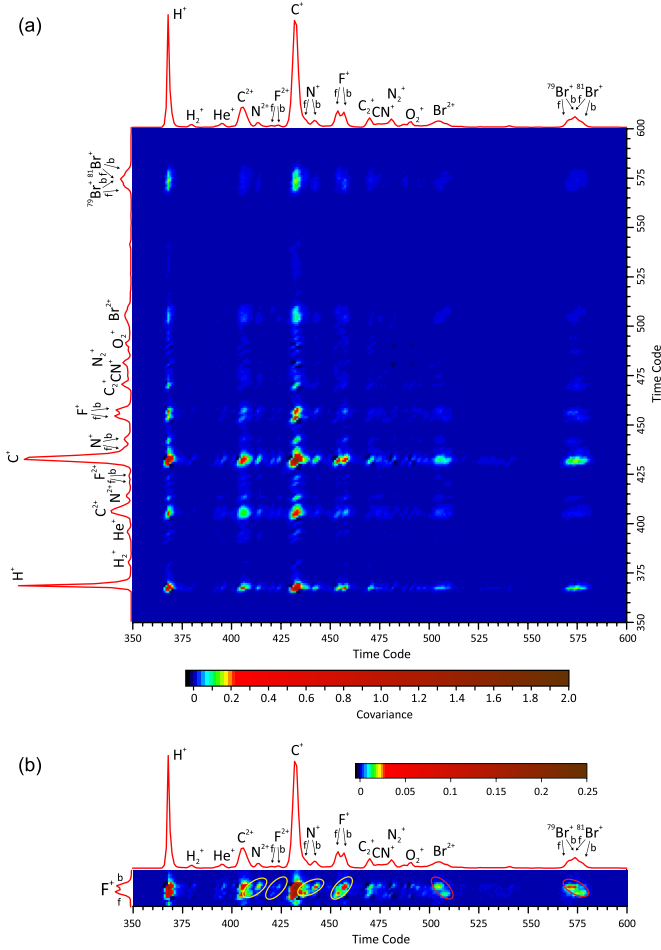


FIG. 4. (Color online) Time-of-flight covariance map: (a) full covariance between all time codes, as calculated from the PIMMS data. The autocorrelation normally present in such a measurement is not present as the correlation of each particle with itself has been ignored. (b) A magnified detail of the full covariance plot in (a) corresponding to the correlations of F^+ ions to all others in the spectrum. The rings highlight asymmetric correlations in the data.

The covariance may be formulated as [40]

$$C(x, y) = \langle X(x)Y(y) \rangle - \langle X(x) \rangle \langle Y(y) \rangle \quad (1)$$

$$= \frac{1}{N} \sum_{i=1}^N X_i(x)Y_i(y) - \left[\frac{1}{N} \sum_{i=1}^N X_i(x) \right] \times \left[\frac{1}{N} \sum_{i=1}^N Y_i(y) \right], \quad (2)$$

where the expectation values $\langle \cdot \rangle$ are calculated over N laser shots. Equation (2) may be applied to the measurement of correlations between the times of flight, as demonstrated by Frasninski *et al.* [37]. In this case, X and Y are simply the same time-of-flight spectrum, where $X_i(x)$ is the value of spectrum X at time x on laser shot i . The calculation of the covariance in this way reveals correlations between the mass peaks, which are hidden in the time-averaged spectra considered so far.

Figure 4(a) shows the results of such a covariance analysis on the present data. The contributions from O_2^+ , N_2^+ , H_2^+ ,

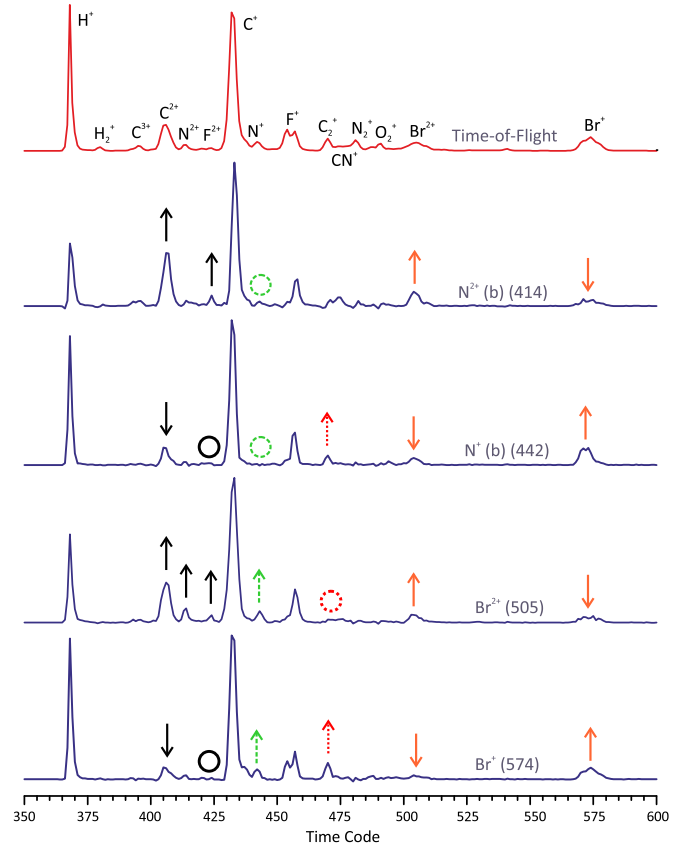


FIG. 5. (Color online) Selected traces from the time-of-flight 2D covariance map (Fig. 4). The ion species to which each trace corresponds is labeled along with the time code. The addition of a (b) indicates that a backward-scattered peak has been selected. The top trace is the integrated time-of-flight spectrum, which is included for comparison. The vertical scales have been normalized such that the most intense peak in each trace has a maximum value of 1. The up (down) arrows indicate whether peaks are enhanced (suppressed) relative to the integrated time-of-flight spectrum, and the circles represent the near absence of ion signal.

and He^+ do not correlate with any of the other signals; as expected, their formation is independent of the Coulomb explosion of the biphenyl molecule. The full covariance map presented in Fig. 4(a) is clearly rich in information, and specific details are emphasized in Figs. 4(b) and 5 for ease of discussion.

Figure 4(b) depicts the part of Fig. 4(a) corresponding to correlations involving the F^+ ions in more detail. Asymmetric relationships are found between the forward- and backward-scattered peaks of F^+ , as well as with Br^+ and N^+ , as indicated by the various rings. Comparison with the molecular structure of the parent identifies the cause of these relationships: in perpendicular alignment, if one F^+ ion is found scattered in either the forward or backward direction, the remaining F^+ and N^+ ions must necessarily scatter in the same direction, while the Br^+ ions must scatter in the opposite direction due to their relative location within the parent molecule.

Figure 5 shows some covariance profiles (four lower traces) from Fig. 4(a) for selected time codes corresponding to the different ion species alongside the total time-of-flight spectrum

(upper trace) for comparison. Interestingly, there is a striking difference in the time-of-flight covariance traces for doubly charged ions compared to singly charged ions, as indicated by arrows in Fig. 5. The circles represent the near absence of ion signal at that time code. In particular, the C^{2+} signal is much more strongly correlated to N^{2+} and Br^{2+} than to their singly charged counterparts, as are the F^{2+} and N^{2+} signals (indicated as black solid arrows and circles). Conversely, the Br^+ signal is reduced in favor of Br^{2+} in correlation with N^{2+} and Br^{2+} [orange (gray) arrows]. Similarly, the C_2^+ signal is correlated with the singly charged N^+ and Br^+ but absent in the Br^{2+} trace (red dotted arrows and circle). This observation, that singly and doubly charged ions are found to correlate with one another, suggests that charge is spread relatively evenly over the molecule and that highly localized charge buildup is unlikely: if the overall charge is relatively low, singly charged ions are favored, and it is unlikely that sufficient charge is accumulated on an individual atom to become doubly charged; if the total charge becomes higher, doubly charged ions become increasingly common. Note the absence of N^+ in the N^+ and N^{2+} traces (indicated as green dashed circles), which is expected considering that only a single N atom is present in the parent molecule.

In summary, careful analysis of time-of-flight correlations can reveal considerable structural information about the molecule, for instance, the presence of a single N but multiple F and Br atoms and opposing locations of the F (and N) atoms and the Br atoms within the parent molecule, and it also reveals details of the Coulomb explosion process, such as the relatively even charge buildup within the molecule prior to fragmentation.

B. From laboratory-frame ion images to recoil-frame covariance images

1. Covariance analysis of ion images

The covariance method is not limited to measuring correlations between the time coordinates of the ion events recorded by the PImMS camera and may also be applied to the measurement of correlations in the full (x, y, t) coordinate space recorded by the sensor. In this way, it is possible to measure correlations between the various ion photofragment velocity vectors [3,41–43]. In practice, it is unnecessary to use the full (x, y, t) information, and the data become more informative if the ion events are grouped according to the ion species attributed to each time code. Following this approach, the t coordinate is replaced by an ion identification. For example, any event that occurs within the time code window 567–581 in the perpendicularly aligned data set is identified as a Br^+ ion. In the present example, this reduces the 4095 individual time codes present in the PImMS data down to fewer than 10 ion species of interest. In this case, $X_i(x)$ in Eq. (2) is the value of the PImMS data set for ion species X at spatial coordinate x , as recorded on laser shot i . Using this formulation, the covariance analysis can be applied to the signal variations recorded by each pixel of the sensor for either the same or two different ionic photofragments, X and Y . However, for each pair of ions between which the covariance is measured, there still exists an overwhelming amount of covariance data. For each pair of ions there will exist $N^4/2$

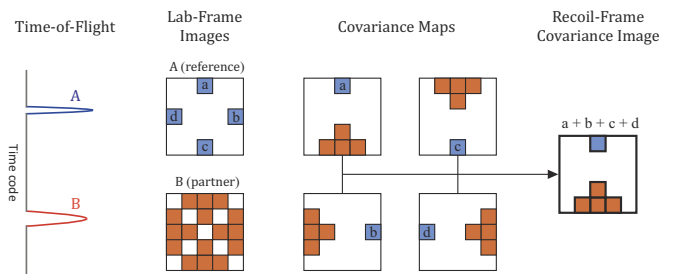


FIG. 6. (Color online) Illustration of the various stages involved in the generation of a recoil frame covariance image. First, two time windows corresponding to two ion species, A and B, are identified. One of the ions is designated the “reference” ion, in this case ion A. The covariance maps plotting the correlation of each pixel in the reference frame (pixels a–d) to each pixel in the partner frame are generated. Each of these covariance maps is rotated so that the velocity of the reference ion is confined to a single vector, and they are summed together to produce a recoil-frame covariance image.

individual correlation measurements for a sensor consisting of $N \times N$ pixels, where the factor of 2 accounts for the reciprocal nature of the covariance. It is therefore necessary to develop methods for condensing the data into a more manageable form.

A particularly intuitive representation is to transform the coordinate system of the measurements, such that the data are presented in the recoil frame of one of the ion species between which covariances are being measured. In this approach, one ionic species is designated as the “reference” ion, and the covariance between each pixel in the reference-ion time window and each pixel in the partner ion time window is calculated. In this way, each pixel of the sensor has an associated “covariance map,” showing the correlations of the reference ions at that pixel to the partner ions recorded by each pixel of the sensor. The covariance maps for each pixel are then rotated such that the reference pixels all lie along a common vector and are summed together. This results in a recoil-frame covariance image or covariance map, in which the velocity vectors of the reference ions are confined along a single direction, and the covariances with the partner ions are shown relative to this vector. This visual representation of the two-vector correlations is a useful and intuitive tool through which the features and trends in the data can be more readily appreciated.

Figure 6 illustrates schematically the various stages involved in the production of a recoil-frame covariance image. In this case the reference-ion velocity vector, with respect to which the correlations are measured, is rotated such that the x component of the velocity is zero and the y component is positive; that is, the reference-ion velocity vector lies vertically along the line connecting the center of the image with the top edge. For each of the recoil-frame covariance images presented here, this is the frame of reference that is used.

2. Overview of all covariance images

The full extent of the information provided by performing two measurement series, comprising around 2.5 hours total collection time, can be appreciated from inspection of Fig. 7. Importantly, the two orthogonal projections of the ion

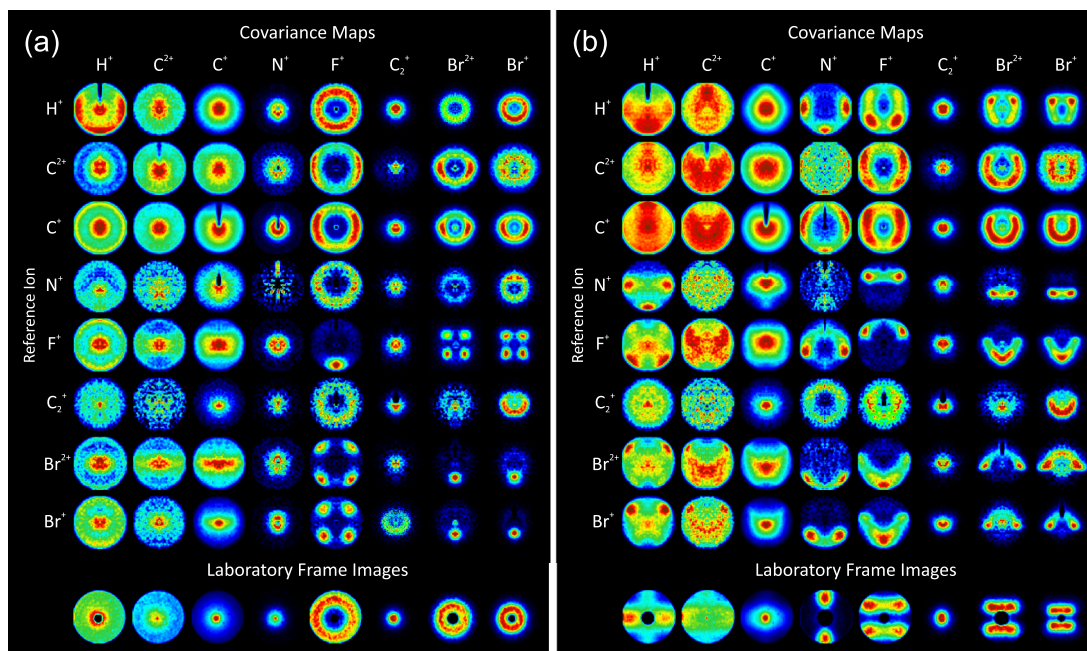


FIG. 7. (Color online) Covariance images obtained in (a) perpendicular and (b) parallel alignment for each ion species (labeled at the top) relative to various reference ions (labeled at the left). In each case the reference ion is confined to a vertical vector from the center of the covariance image to the top edge. The covariance images are compared to the laboratory-frame ion images (shown at the bottom of each panel).

trajectories afforded by the adiabatic alignment of the target molecules provide complementary structural and dynamical information. Each geometry yields 63 individual covariance maps, representing the two-vector velocity correlations between each pair of product ions (excluding the physically impossible N^+ autocorrelation map). When compared to the information content of the uncorrelated laboratory frame measurements, the advantage of considering the velocity vector correlations is clear. The majority of the covariance images show distinctly anisotropic distributions, which relate directly to the structure of the molecules prior to Coulomb explosion and to the dynamics of the dissociation process.

It is perhaps unsurprising that clear and distinct anisotropies are present in some of the covariance images, particularly those between peripheral substituents occupying a limited number of positions in the molecule. However, it is interesting that even the covariance images corresponding to the 13 carbon atoms comprising the molecular skeleton (C^+ and C^{2+}) are highly structured. In the case of H^+ ions, each covariance image has a unique and complex structure, containing important information about the connectivity of the atoms in the parent molecule and the Coulomb explosion dynamics.

3. Detailed analysis of selected covariance images

A detailed discussion of the relationships between the parent molecular structure and the covariance images of F^+ and Br^+ relative to N^+ in parallel alignment and of F^+ and Br^+ relative to one another in perpendicular alignment has been presented in a previous publication [9] and will not be revisited here. In this section we expand the discussion to consider a broader range of correlations, highlighting the clear relationships between the parent molecular structure and the fragment-ion recoil trajectories.

a. H^+ with respect to N^+ in parallel alignment. The laboratory-frame image of H^+ [Fig. 8(a)] in parallel alignment already displays significant structure, with the majority of the signal directed at 90° to the alignment laser pulse (vertical in this case); these signals can be related to the four hydrogen atoms situated around the waist of the molecule. The only other hydrogen atom is situated at the tip of the molecule, opposite the CN group, and causes the weaker signal around 0° and 180° in the laboratory-frame image due to the lack of preferential orientation of the parent molecules. When the hydrogen signal

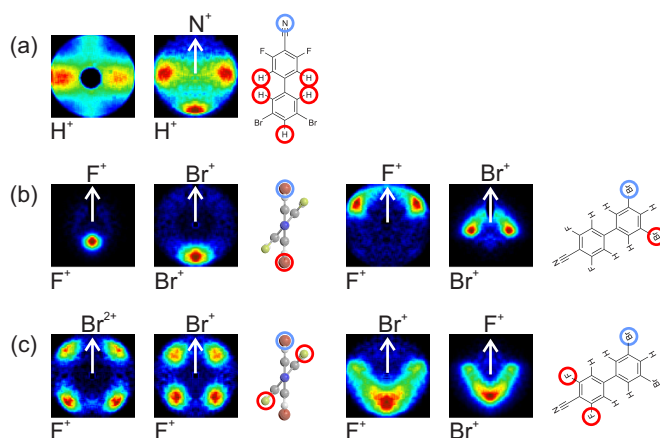


FIG. 8. (Color online) (a) Laboratory-frame image of H^+ and covariance image of H^+ with respect to N^+ in parallel alignment. (b) F^+ with respect to F^+ and Br^+ with respect to Br^+ in perpendicular (left) and parallel alignment (right). (c) F^+ with respect to Br^{2+} compared to F^+ with respect to Br^+ in perpendicular alignment (left). Also shown are F^+ with respect to Br^+ and Br^+ with respect to F^+ in parallel alignment (right).

is measured in correlation with N^+ and rotated into the recoil frame, the covariance image resembles that expected in the laboratory frame for perfectly oriented parent molecules.

b. F^+ with respect to F^+ and Br^+ with respect to Br^+ in perpendicular alignment. Figure 8(b) shows the covariance image of F^+ with respect to F^+ (i.e., autovariance). As the two F atoms sit on opposite sides of the phenyl ring, as seen in the relevant projection for perpendicular alignment shown in the left panel of Fig. 8(b), the maximum covariance intensity is located at 180° in the covariance image, directly opposing the trajectory of the reference ion, which is traveling towards the top of the image (0°). The same applies to the covariance image of Br^+ with respect to Br^+ , also shown in left panel of Fig. 8(b).

c. F^+ with respect to F^+ and Br^+ with respect to Br^+ in parallel alignment. By comparison, the covariance images of F^+ with respect to F^+ and of Br^+ with respect to Br^+ in parallel alignment illustrate the relative positions of the partner atoms in the orthogonal projection, as illustrated in the right panel of Fig. 8(b). In both covariance images, the angle between the peak covariance and the reference ion compares well with the molecular structure. Additional features in the covariance images are due to free rotations of the molecule about the MPA when 1D aligned.

d. F^+ with respect to Br^{2+} compared with F^+ with respect to Br^+ in perpendicular alignment. The specific case of F^+ with respect to Br^+ (and vice versa) in perpendicular alignment has been discussed in detail in a previous publication [9] and has been shown to be a good indicator of the dihedral angle between the two phenyl rings. As a further point, it is interesting to examine the different velocity profiles of F^+ in coincidence with Br^+ and Br^{2+} , as illustrated in the left panel of Fig. 8(c). This finding is in good agreement with the discussion in Sec. III A 3: if the bromine partner ion is doubly charged, the parent molecule is likely to have been in a high overall charge state, and the fragments, including those that are singly charged, obtain a higher kinetic energy due to increased pairwise Coulomb forces, which manifests as a larger radius in the covariance images. This trend is repeated for other ion pairs, with the same effect also observed in the covariance images measured relative to C^+ and C^{2+} .

e. F^+ with respect to Br^+ and Br^+ with respect to F^+ in parallel alignment. While the covariance image of F^+ with respect to Br^+ in perpendicular alignment is interesting for its correlation with the dihedral angle, the case of F^+ with respect to Br^+ in parallel alignment is more challenging to interpret. The right panel of Fig. 8(c) shows the covariance image of F^+ with respect to Br^+ in comparison to the molecular structure (in parallel-alignment projection) rotated such that the Br reference is pointing towards the top, as is the case in the recoil frame if assuming approximately axial recoil of the fragment ions. The signal location in the covariance image is in good agreement with the relative positions of the F atoms. The signal at 180° is stronger than those around 60° and 300° , as one of the F^+ ions always recoils in an antiparallel manner relative to the reference Br^+ ion, while the second F^+ ion can be located on either side. The same considerations apply to the covariance image of Br^+ with respect to F^+ [right panel of Fig. 8(c)]: the general form of the signal is very similar, for the same reasons.

The above discussion, coupled with previously presented data [9], demonstrates that it is possible to infer details of the parent molecular structure and of the Coulomb-explosion process directly from the covariance images themselves. When combined with the laboratory-frame ion images and the time-of-flight covariance maps, an increasingly detailed picture of the fragmentation dynamics is revealed.

However, it is clear that in order to pursue a more quantitative interpretation of the data, in terms of both the structure of the parent molecule and the dynamics of ionization and subsequent Coulomb explosion, some model of the system must be constructed to guide and support more detailed inferences. The following sections therefore explore the application of a simple classical model of Coulomb explosion to the experimental data.

C. Simulations of Coulomb-explosion ion trajectories

1. Computational details

Coulomb explosion is a highly complex process, involving ionization, charge redistribution, and molecular breakup, all occurring on competing time scales of a few tens of femtoseconds. Furthermore, the presence of the intense laser field used to induce ionization may have unintended consequences for the structure of the target molecules beyond simple removal of valence electrons. However, as an initial approximation, the Coulomb-explosion process may be modeled through simple classical trajectory calculations of point charges following instantaneous ionization of the parent molecule. While such an approximation ignores many of the important details of ionization, charge transfer, and structural deformation that may occur during the initial phases of Coulomb explosion, the success, or otherwise, of this simple model in simulating the experiment is useful as a guide towards a more detailed interpretation of the data and the underlying processes that characterize Coulomb explosion. More specifically, several approximations have been made in the model used to calculate the ion trajectories:

- (i) All atoms within the molecule are assumed to be stationary immediately prior to Coulomb explosion.
- (ii) The position of each atom within the molecule is defined by the equilibrium geometry of the molecule, as determined from the density-functional-theory calculations [44,45].
- (iii) The motion of the ions is assumed to be entirely governed by the interionic forces of Coulomb repulsion, with no contribution from the bonding characteristics of the molecule. No allowance is made for interactions between ions and neutral fragments, nor do the simulations allow for the creation of molecular fragment ions.
- (iv) The charge distribution within the molecule is well defined; that is, a fixed number of charges is assigned to each atom at the start of the simulation with no charge redistribution occurring thereafter.

Under these conditions, the trajectories of the ions are described by a set of coupled second-order differential equations of the form

$$M_i u \frac{d^2 x_i}{dt^2} = \sum_{j \neq i}^N \frac{z_i z_j e^2 (x_i - x_j)}{4\pi \epsilon_0 |x_i - x_j|^3} \quad (3)$$

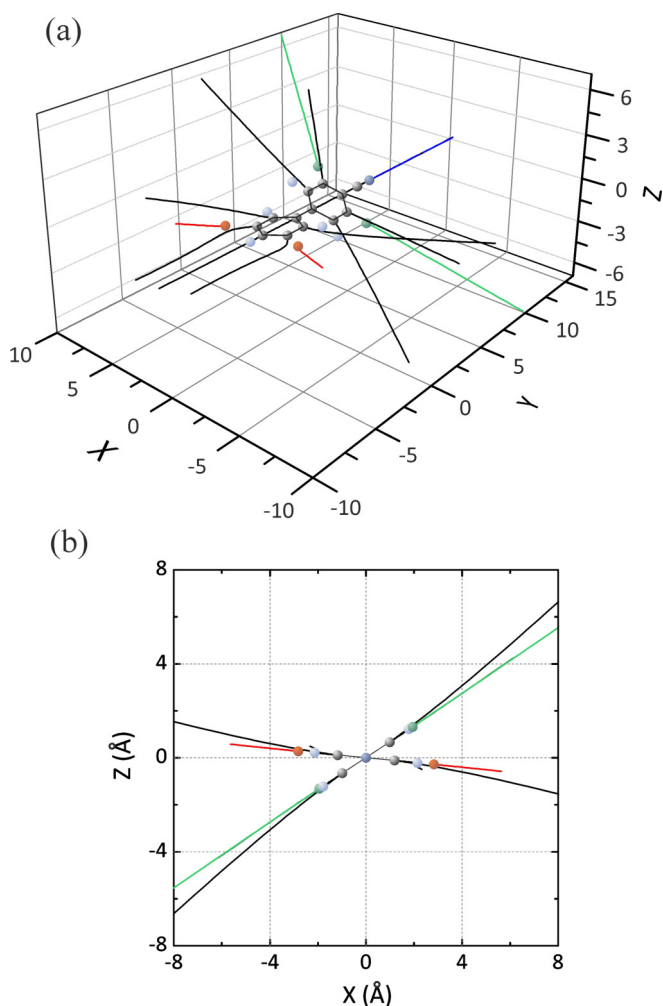


FIG. 9. (Color online) Plots of the trajectories of the fragment ions following Coulomb explosion of DBrDFCNBph carrying a single positive charge on each atom (a) in three dimensions, with axis units in angstroms, and (b) as projected onto the xz plane, where the y axis is coincident with the C_2 symmetry axis of the molecule. The trajectories are plotted up to 70 fs after the start of the simulation.

for $i = 1, \dots, N$, with M_i , z_i , and x_i being the mass, charge, and position of atom i , respectively, and u and e being the atomic mass unit and elementary charge. These equations are solved numerically using an ordinary differential equation (ODE) solver contained in the library of commercially available software (MATLAB) to yield $x_i(t)$ for all i [46].

2. Simulated ion trajectories

Figure 9 shows simulated ion trajectories of atomic fragment ions from the biphenyl parent molecule after Coulomb explosion with a single positive charge assigned to each atom in the molecule.

While this particular charge configuration is unlikely to be representative of the actual charge distribution in the molecule, the trajectories that result are a useful guide for understanding the dynamics of the Coulomb explosion process and the interactions between the various ionic photofragments. The calculated ion trajectories illustrate that, while for some atoms (such as the peripheral substituents N, F, and Br) axial recoil

does indeed serve as a reasonable approximation, for a number of the constituent atoms, particularly those from the core of the parent molecule, the trajectories depart substantially from the axial recoil scheme. This observation is particularly noticeable in the case of the two C^+ ions originally bonded to the Br atoms. As the heavier, and therefore slower-moving, Br^+ ions obstruct the recoiling C^+ , the C^+ trajectories are deflected towards the long axis of the molecule, finally traveling almost parallel to the trajectory of the C^+ from the tip of the molecule.

Figure 9(b) shows the projection of the ion trajectories onto the xz plane, where the y axis is coincident with the MPA of the molecule. Interestingly, the halogen substituents leave the molecule along trajectories largely confined to the planes defined by the two phenyl rings to which they are originally bonded. This suggests that the relative recoil of the Br^+ and F^+ , as imaged in the xz plane, is indeed indicative of the dihedral angle, as proposed in previous publications [9,19].

3. Simulating ensembles

The simulated final velocities of the ionic fragments in the detector plane may be used to construct simulated velocity-map ion images. In order to simulate more closely the experimental data, several modifications were made to the simulation routine. The simulations presented in Fig. 9 were concerned with the Coulomb explosion of a single parent molecule, whereas the experimental images are averaged over very many molecular configurations and charge states. To more accurately model this in the simulations, ion trajectories must be sampled from the appropriate distribution of starting conditions.

In the experiment, the 1D aligned molecules are free to rotate around the C_2 symmetry axis, which is accounted for in the simulations by rotating each molecule by a random angle about this axis prior to Coulomb explosion. The imperfect degree of alignment of molecules under experimental conditions is also taken into account by using a distribution of angles between the MPA of the molecule and the polarization axis of the alignment laser pulse. Specifically, this is approximated by a $\cos^4 \theta$ distribution, where θ is the angle between the electric vector of the alignment laser pulse and the C_2 symmetry axis of the molecule, although it is recognized that the precise form of the angular distribution will depend on the rotational states populated and laser field strength [47].

In addition to molecular alignment considerations, the total charge of the parent molecule prior to Coulomb explosion and the distribution of these charges among the constituent atoms must be more accurately simulated, rather than simply assuming a single charge per atom as has been the case thus far. This is done by assigning each molecule an integer number of positive charges according to a Poisson distribution, with an average value of 15 charges per molecule found to give the closest fit to the experimental data. This estimate of the number of charges per molecule is broadly consistent with a statistical analysis of the experimental data based on the number of ion events detected per laser shot and the estimated detection efficiency of the ions. The charges are randomly localized among the atoms, weighted according to the experimentally observed relative charge per atom type, as observed from the time-of-flight data. Additionally, each atom type has a

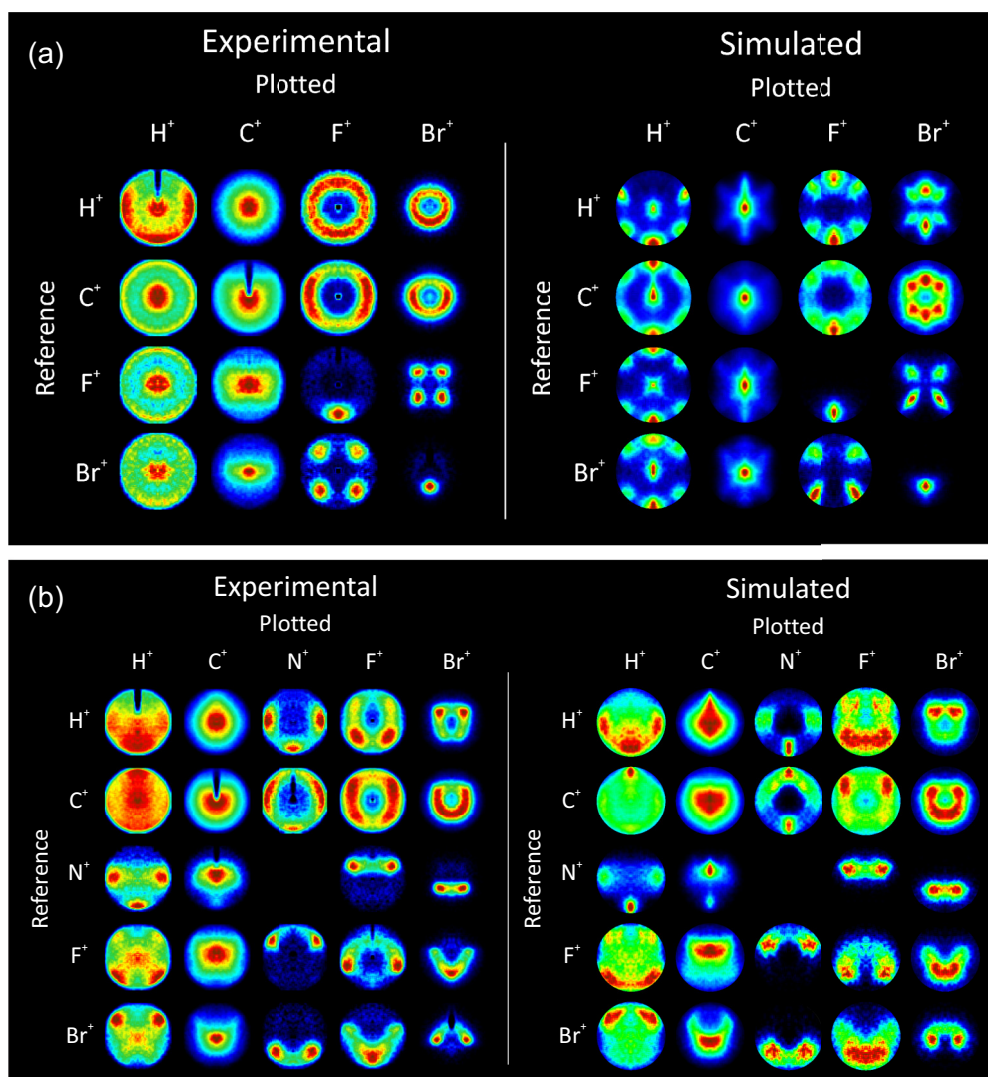


FIG. 10. (Color online) (left) Experimental and (right) simulated recoil-frame covariance images recorded in (a) perpendicular and (b) parallel alignment. In each case the ion species plotted is labeled at the top of the column, with the reference ion labeled to the left of the rows. The reference ion is confined to a vertical vector from the center of the covariance image to the top edge. Only the covariances involving singly charged ions are shown. Covariance maps involving N^+ in the perpendicular geometry are not very informative due to the central location of the N atom in the molecule when viewed in this alignment, and they are therefore not shown in (a).

maximum number of charges that it may support, assumed fixed throughout the fragmentation process, as informed by the time-of-flight data ($H = 1$; $C, N, F = 2$; $Br = 3$).

With these additional layers of averaging included in the ion-trajectory simulation routine, it becomes possible to attempt a full simulation of the experiment. Each simulation is run over 30 000 trajectories in order to achieve a satisfactory convergence of the data, and the coincidence maps generated on each iteration are summed together to yield the final output.

Figure 10 compares experimental and simulated covariance images for parallel [Fig. 10(a)] and perpendicular [Fig. 10(b)] alignment. In perpendicular alignment it is immediately obvious that the agreement between the simulated and experimental data is, at least qualitatively, very good. In general, the majority of the experimentally observed features are clearly reproduced in the simulated recoil-frame covariance images. The strength of the agreement is perhaps surprising, given the simple assumptions of the model and the relatively long duration of

the probe laser pulse. The simulations suggest that the variable initial charge state of the target molecules is largely responsible for the broad nature of the features present in the experimental covariance images, with further broadening caused by the finite degree of alignment of the target molecules and free rotation about the MPA.

In perpendicular alignment the F^+ and Br^+ covariance signals, discussed further in Sec. III C 4, are generally very well accounted for by the simulations. However, in general the simulations in the perpendicular alignment geometry appear to be somewhat less successful in reproducing the features of the experimental covariance images than in the parallel alignment. Although the radial properties of the simulated covariance images are generally in good agreement with the experimental data, the angular properties are somewhat less convincingly reproduced than in the case of parallel alignment. The features of the simulated covariance images are considerably more localized than those present in the experimental data,

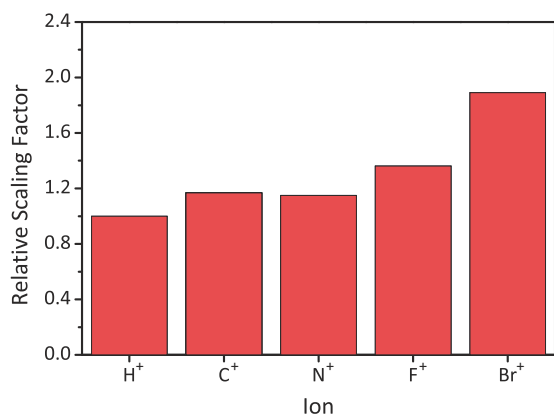


FIG. 11. (Color online) Relative average scaling factors used for the simulated recoil-frame covariance images of each ion species. See text for details.

suggesting a far higher degree of angular correlation between the fragment ions than is observed experimentally. The relatively low level of angular correlation observed experimentally is perhaps suggestive of deformation of the parent molecule out of the planes defined by the phenyl rings during the early stages of Coulomb explosion. This result should perhaps be expected given that the phenyl rings are initially planar to facilitate the delocalization of π electrons, which are likely to be removed during the process of ionization preceding molecular explosion. With the stabilizing effect of conjugation lost, the molecule is free to relax into a nonplanar conformation. Such a relaxation of the initially rigid carbon skeleton would have the result of reducing the strength of the angular correlations between the trajectories of the fragment ions, as observed in the experimental data. The angular correlations observed following alignment of the MPA perpendicular to the imaging plane are far more sensitive to the planarity, or otherwise, of the phenyl rings than the measurements taken in a parallel geometry, hence the somewhat poorer agreement between the simulated and experimental data in this case. Nevertheless, certain covariance images show a clear similarity between the simulated and experimental data. In particular, the covariance images describing correlations involving F⁺ and Br⁺ resemble closely those predicted by the simulations. Since these correlations are indicative of the dihedral angle between the two phenyl rings, it is noteworthy that the simulations successfully reproduce the experimental data in these cases.

In the course of performing the simulations it was found necessary to scale the simulated velocities in order to obtain a best match with the experiment. Figure 11 summarizes these average relative scaling factors used to match the simulated velocity data to the experimental covariance images for each ion species. The scaling factors reveal some interesting discrepancies between the simulated and experimental data. Clearly, the bromine ion velocities observed experimentally are far in excess of those predicted through simulation. This might be suggestive of substantial charge migration during the early stages of Coulomb explosion. In the ion-trajectory calculations the initial charge state of each ion is conserved throughout the simulation. In order to account for the experimentally observed bromine ion velocities, it would

appear that the ions might initially carry a far higher charge than is observed at the detector such that the ions possess sufficient Coulombic potential energy to account for their final recoil velocities. This hypothesis appears to be supported by preliminary electron density calculations presented in Ref. [48], which predict partial charges on each of the bromine ions to be considerably in excess of those observed experimentally from the ion yields. One possible explanation might be that in the molecular ion the positive charge is carried to a substantial degree by the bromine atoms and is redistributed during the early stages of fragmentation to yield the observed charge states of the bromine ions. It is also worth bearing in mind that the detailed role of the YAG pulse is yet to be established. The H⁺ scaling factors are the lowest of all ions. This may be explained by considering that the hydrogen ions are expected to become substantially displaced on the time scale of molecular ionization due to their low mass, thereby reducing the final velocities of the ions from those expected based on an impulsive ionization model. That the scaling factor is not very much smaller than the other ions is perhaps surprising and suggests that the hydrogen atoms remain bound to the molecule for a substantial time during the process of ionization. The scaling factors of the remaining ions lie somewhere between these two limits. The slightly higher scaling factors applied to the fluorine-ion images are perhaps suggestive of some degree of charge redistribution akin to that observed for the bromine ions but to a far lesser extent.

4. Quantitative comparison of simulated and experimental data

In recent publications we have used the F⁺ and Br⁺ covariance signals in perpendicular alignment to estimate the dihedral angle of the biphenyl molecule [3,9] and subsequently to follow torsional motion in real time [3,19], effectively producing a molecular movie of the motion. It is therefore interesting to pursue a quantitative comparison of experimental and simulated data in this particular case to establish the reliability of the method in providing information about the torsional angle in the parent molecule.

Figure 12(a) compares the experimental and simulated covariance images reflecting correlations between F⁺ and Br⁺ in perpendicular alignment. Below the images, the correlation strength is plotted as a function of the relative angle between the probe and the reference ion. It is striking that both curves peak at similar angles. From a fitting of the simulated data to four asymmetric sigmoidal peak functions, the most probable relative recoil angles between the F⁺ and Br⁺ ion fragments are found to be $48.3^\circ \pm 2.3^\circ$ for the near-side peaks, for which the ion recoil is close to that of the reference, and $137.2^\circ \pm 1.5^\circ$ for the far-side peaks, for which the ion recoil is close to opposite that of the reference, corresponding to a dihedral angle of $42.8^\circ \pm 1.5^\circ$. These values are in good agreement with those measured from the experimental data, in which the maxima are observed at $45.1^\circ \pm 0.4^\circ$ for the near-side peaks and at $138.2^\circ \pm 1.3^\circ$ for the far-side peaks, corresponding to a dihedral angle of $41.8^\circ \pm 1.3^\circ$.

In addition to accurately predicting the relative recoil angles of the F⁺ and Br⁺ product ions, the differences observed between the near-side and far-side peaks are also reproduced in the simulated data, with the far-side peaks being

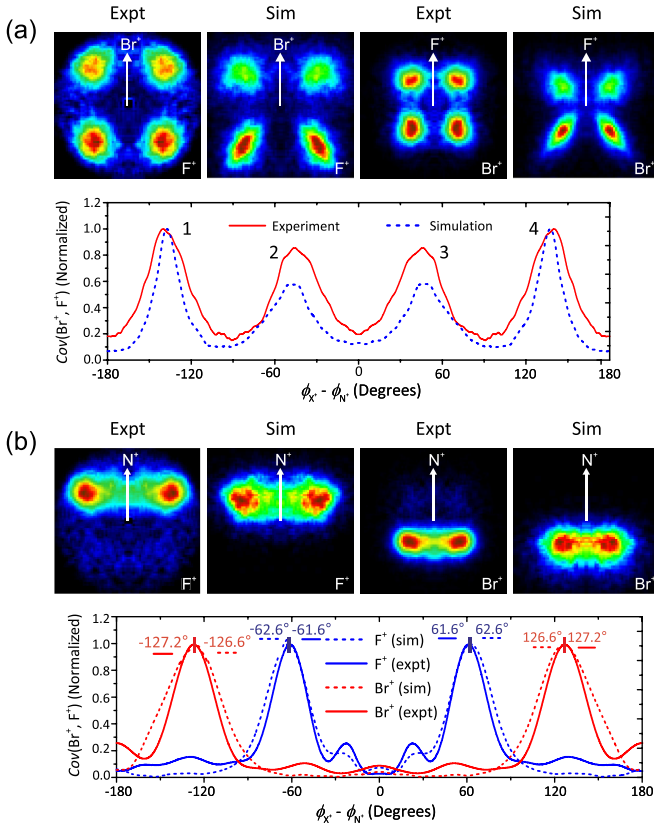


FIG. 12. (Color online) Comparison of selected experimental and simulated covariance images in (a) perpendicular and (b) parallel alignment. Presented in (a) are covariance images of F^+ relative to Br^+ and Br^+ relative to F^+ as indicated. The panel below the images compares the simulated (dashed line) and experimental (solid line) covariance as a function of the relative recoil angle of the partner fragment ions. Presented in (b) are the experimental and simulated covariance images of F^+ relative to N^+ and Br^+ relative to N^+ . The panel below the images compares the simulated (dashed line) and experimental covariance (solid line) as a function of the relative recoil angle of the partner fragment ions, as determined from pBASEX inverted data presented previously [9].

considerably narrower and implying a smaller dihedral angle than their near-side counterparts. In a previous publication [9] we suggested that this difference is likely due to the increased pairwise Coulomb repulsion experienced between the F^+ and Br^+ fragment ions when the two ions originate from the same side of the molecule. Since the model exclusively considers Coulombic interactions between ions, that such features are present in the simulated covariance images validates this assertion.

Figure 12(b) compares the experimental and simulated covariance images of F^+ (left) and Br^+ (right) in parallel alignment, both with N^+ as the reference ion. Below the images, the correlation strength is plotted as a function of the relative angle between the probe and the reference ion, following an Abel inversion of the covariance images (see Ref. [9] for details). The close similarity between the experimental and simulated data is reflected in the angular distributions: the covariance intensity peaks at almost exactly the same angles (experimental $\pm 61.6^\circ$, simulated $\pm 62.6^\circ$ for

F^+ ; experimental $\pm 127.2^\circ$, simulated $\pm 126.6^\circ$ for Br^+). The level of agreement between the experimental and simulated data is surprisingly good, given the simplicity of the model employed and the approximations involved. However, there remain some significant differences between the experimental and simulated data, most notably in the relative spread of recoil velocities of the photofragments and the degree of confinement about the most probable relative recoil angles.

IV. CONCLUSIONS AND FUTURE PERSPECTIVES

We have demonstrated that the application of a PImMS camera to the recording of multimass velocity-map images following the Coulomb explosion of a large prealigned polyatomic molecule provides detailed information on the correlated velocity distributions of the fragment ions. Analysis of the correlated fragment-ion trajectories provides insight into the structure of the parent molecule and the dynamics of Coulomb explosion. The measured and simulated fragment-ion trajectories obtained in this work suggest that it is indeed possible to measure to a reasonable degree of accuracy various characteristic structural coordinates of the parent system on a femtosecond time scale.

The experiments we have presented use 1D adiabatic alignment of the target molecules prior to Coulomb explosion to aid the interpretation of the experimental data. While it is arguably not entirely necessary to pursue such a scheme, the advantages of this approach are clear. In the present example, the MPA of the molecules coincides with the primary molecular axis, allowing for a straightforward interpretation of the resulting ion images and covariance information. However, while it will often be the case that the most polarizable axis coincides with a useful reference access within the molecule, this is by no means guaranteed, which has implications for the range of systems for which the combination of alignment and CEI is suitable. The relatively long ionizing laser pulse is also likely to cause a reduction in the information content of the resulting data, with minor rearrangements of the parent structure possible on the time scale of the ionization process. Commercial systems are currently available that provide laser pulses as short as a few femtoseconds, which limits the possibilities for atomic motion during the ionizing step of Coulomb explosion. This allows for a more accurate determination of the structural coordinates of the parent system, including the possibility of measuring bond lengths in addition to bond angles and molecular configuration.

The success of a simple model in the simulation of the ion trajectories is encouraging. The details of the simulations reveal much about the dynamics of Coulomb explosion and are informative of the relationship between the structure of the parent molecule and the final trajectories of the various fragment ions. This simple model could be refined to include, for example, the effects of charge migration during the early stages of the Coulomb explosion, different ionization probabilities for the various atom types, a more sophisticated treatment of the imperfect molecular alignment, and a detailed description of the role of the YAG pulse. Such refined simulations would be useful to further our understanding of the interesting and complex phenomenon of Coulomb explosion. That such a simple model has proved capable of reproducing many of the characteristic features present in the experimental

data suggests that there is much promise in the suggestion that CEI combined with ion-trajectory calculations represents a relatively straightforward and accessible means of monitoring structural parameters of molecular systems on a femtosecond time scale. Furthermore, that the simulations predict to a reasonable degree of accuracy the trajectories of even the lightest ions following Coulomb explosion involving both probe and YAG laser pulses is surprising. The success of the model strongly suggests that all ionization and fragmentation processes occur on a very short time scale, which allows the correlations between fragments to be preserved during Coulomb explosion.

In a related publication by the authors, the methods employed here are further exploited to measuring the time-resolved torsional motion, reflected in time-dependent changes in the dihedral angle following excitation of the torsional mode by a femtosecond “kick” pulse [19]. More generally, the strategy introduced in this paper holds considerable promise

for the measurement of characteristic structural parameters, particularly those relating to bond angles, of relatively large polyatomic systems on a femtosecond time scale.

ACKNOWLEDGMENTS

H.S. acknowledges an ERC-AdG (Project No. 320459, DropletControl), the Lundbeck Foundation, the Carlsberg Foundation, and the Danish Council for Independent Research (Natural Sciences). M.P.J. acknowledges CSC. The Finnish IT Center for Science hosted parts of the calculations. M.B. and C.V. acknowledge the support of the EPSRC via Programme Grant No. EP/L005913/1, the EU through grant FP7 ITN “ICONIC” (Project Grant No. 238671), STFC through a PNPAS award and a mini-IPS grant (ST/J002895/1), and a proof-of-concept grant from ISIS Innovation Ltd. A.L. thanks the DFG for support, via Grants No. LA 3209/1-1 and No. LA 3209/1-2.

-
- [1] H. Stapelfeldt, E. Constant, and P. B. Corkum, *Phys. Rev. Lett.* **74**, 3780 (1995).
 - [2] T. Ergler, A. Rudenko, B. Feuerstein, K. Zrost, C. D. Schröter, R. Moshhammer, and J. Ullrich, *Phys. Rev. Lett.* **97**, 193001 (2006).
 - [3] J. L. Hansen, J. H. Nielsen, C. B. Madsen, A. T. Lindhardt, M. P. Johansson, T. Skrydstrup, L. B. Madsen, and H. Stapelfeldt, *J. Chem. Phys.* **136**, 204310 (2012).
 - [4] K. Codling and L. Frasinski, *J. Phys. B* **26**, 783 (1993).
 - [5] A. Rudenko, T. Ergler, B. Feuerstein, K. Zrost, C. Schröter, R. Moshhammer, and J. Ullrich, *Chem. Phys.* **329**, 193 (2006).
 - [6] F. Légaré, K. F. Lee, I. Litvinyuk, P. Dooley, S. Wesolowski, P. Bunker, P. Dombi, F. Krausz, A. Bandrauk, D. Villeneuve, and P. Corkum, *Phys. Rev. A* **71**, 013415 (2005).
 - [7] J. Gagnon, K. F. Lee, D. M. Rayner, P. B. Corkum, and V. R. Bhardwaj, *J. Phys. B* **41**, 215104 (2008).
 - [8] M. Pitzer, M. Kunitski, A. Johnson, T. Jahnke, H. Sann, F. Sturm, L. Schmidt, H. Schmidt-Böcking, R. Dörner, J. Stohner, J. Kiedrowski, M. Reggelen, S. Marquardt, A. Schießer, R. Berger, and M. Schöffler, *Science* **341**, 1096 (2013).
 - [9] C. S. Slater, S. Blake, M. Brouard, A. Lauer, C. Vallance, J. J. John, R. Turchetta, A. Nomerotski, L. Christensen, J. H. Nielsen, M. P. Johansson, and H. Stapelfeldt, *Phys. Rev. A* **89**, 011401(R) (2014).
 - [10] A. Faibis, W. Koenig, E. Kanter, and Z. Vager, *Nucl. Instrum. Methods Phys. Res., Sect. B* **13**, 673 (1986).
 - [11] J. A. Davies, J. E. LeClaire, R. E. Continetti, and C. C. Hayden, *J. Chem. Phys.* **111**, 1 (1999).
 - [12] O. Jagutzki, A. Cerezo, A. Czasch, R. Dörner, M. Hattas, M. Huang, V. Mergel, U. Spillmann, K. Ullmann-Pfleger, T. Weber, H. Schmidt-Böcking, and G. Smith, *IEEE Trans. Nucl. Sci.* **49**, 2477 (2002).
 - [13] J. Ullrich, R. Moshhammer, A. Dorn, R. Dörner, L. P. H. Schmidt, and H. Schmidt-Böcking, *Rep. Prog. Phys.* **66**, 1463 (2003).
 - [14] H. Stapelfeldt and T. Seideman, *Rev. Mod. Phys.* **75**, 543 (2003).
 - [15] See the PIMMS website, <http://pimms.chem.ox.ac.uk>.
 - [16] C. Vallance, M. Brouard, A. Lauer, C. S. Slater, E. Halford, B. Winter, S. J. King, J. W. L. Lee, D. E. Pooley, I. Sedgwick, R. Turchetta, A. Nomerotski, J. J. John, and L. Hill, *Phys. Chem. Chem. Phys.* **16**, 383 (2014).
 - [17] A. T. J. B. Eppink and D. H. Parker, *Rev. Sci. Instrum.* **68**, 3477 (1997).
 - [18] D. W. Chandler and P. L. Houston, *J. Chem. Phys.* **87**, 1445 (1987).
 - [19] L. Christensen, J. H. Nielsen, C. B. Brandt, C. B. Madsen, L. B. Madsen, C. S. Slater, A. Lauer, M. Brouard, M. P. Johansson, B. Shepperson, and H. Stapelfeldt, *Phys. Rev. Lett.* **113**, 073005 (2014).
 - [20] U. Even, J. Jortner, D. Noy, N. Lavie, and C. Cossart-Magos, *J. Chem. Phys.* **112**, 8068 (2000).
 - [21] L. Holmegaard, J. H. Nielsen, I. Nevo, H. Stapelfeldt, F. Filsinger, J. Küpper, and G. Meijer, *Phys. Rev. Lett.* **102**, 023001 (2009).
 - [22] A. Nomerotski, M. Brouard, E. Campbell, A. Clark, J. Crooks, J. Fopma, J. J. John, A. J. Johnsen, C. Slater, R. Turchetta, C. Vallance, E. Wilman, and W. H. Yuen, *J. Instrum.* **5**, C07007 (2010).
 - [23] A. Nomerotski, S. Adigun-Boaye, M. Brouard, E. Campbell, A. Clark, J. Crooks, J. John, A. Johnsen, C. Slater, R. Turchetta, C. Vallance, E. Wilman, and W. Yuen, *Nucl. Instrum. Methods Phys. Res., Sect. A* **633**, Suppl. 1, S243 (2011).
 - [24] J. J. John, M. Brouard, A. Clark, J. Crooks, E. Halford, L. Hill, J. W. L. Lee, A. Nomerotski, R. Pisarczyk, I. Sedgwick, C. S. Slater, R. Turchetta, C. Vallance, E. Wilman, B. Winter, and W. H. Yuen, *J. Instrum.* **7**, C08001 (2012).
 - [25] I. Sedgwick, A. Clark, J. Crooks, R. Turchetta, L. Hill, J. J. John, A. Nomerotski, R. Pisarczyk, M. Brouard, S. H. Gardiner, E. Halford, J. Lee, M. L. Lipciuc, C. Slater, C. Vallance, E. S. Wilman, B. Winter, and W. H. Yuen, in *IEEE 10th International Conference on New Circuits and Systems (NEWCAS) 2012, 17–20 June 2012, Montreal, QC* (IEEE, Piscataway, NJ, 2012), pp. 497–500.
 - [26] A. T. Clark, J. P. Crooks, I. Sedgwick, R. Turchetta, J. W. L. Lee, J. J. John, E. S. Wilman, L. Hill, E. Halford, C. S. Slater, B. Winter, W. H. Yuen, S. H. Gardiner, M. L. Lipciuc, M. Brouard,

- A. Nomerotski, and C. Vallance, *J. Phys. Chem. A* **116**, 10897 (2012).
- [27] M. Brouard, E. Halford, A. Lauer, C. S. Slater, B. Winter, W. H. Yuen, J. J. John, L. Hill, A. Nomerotski, A. Clark, J. Crooks, I. Sedgwick, R. Turchetta, J. W. L. Lee, C. Vallance, and E. Wilman, *Rev. Sci. Instrum.* **83**, 114101 (2012).
- [28] J. H. D. Eland, *Meas. Sci. Technol.* **1**, 36 (1990).
- [29] J. H. D. Eland, *Meas. Sci. Technol.* **5**, 1501 (1994).
- [30] J. Becker, K. Beckord, U. Werner, and H. Lutz, *Nucl. Instrum. Meth. Phys. Res., Sect. A* **337**, 409 (1994).
- [31] O. Jagutzki, V. Mergel, K. Ullmann-Pfleger, L. Spielberger, U. Spillmann, R. Dörner, and H. Schmidt-Böcking, *Nucl. Instrum. Methods Phys. Res., Sect. A* **477**, 244 (2002).
- [32] O. Jagutzki, J. Lapington, L. Worth, U. Spillman, V. Mergel, and H. Schmidt-Böcking, *Nucl. Instrum. Methods Phys. Res., Sect. A* **477**, 256 (2002).
- [33] X. Llopart, R. Ballabriga, M. Campbell, and L. Tlustos, *Nucl. Instrum. Methods Phys. Res., Sect. A* **581**, 485 (2007).
- [34] K. Motomura *et al.*, *Nucl. Instrum. Methods Phys. Res., Sect. A* **606**, 770 (2009).
- [35] M. De Gaspari, J. Alozy, R. Ballabriga, M. Campbell, E. Frojdh, J. Idarraga, S. Kulis, X. Llopart, T. Poikela, P. Valerio, and W. Wong, *J. Instrum.* **9**, C01037 (2014).
- [36] T. Poikela, J. Plosila, T. Westerlund, M. Campbell, M. De Gaspari, X. Llopart, V. Gromov, R. Kluit, M. van Beuzekom, F. Zappone, V. Zivkovic, C. Brezina, K. Desch, Y. Fu, and A. Kruth, *J. Instrum.* **9**, C05013 (2014).
- [37] L. Frasinski, K. Codling, and P. Hatherly, *Science* **246**, 1029 (1989).
- [38] W. A. Bryan, J. H. Sanderson, A. El-Zein, W. R. Newell, P. F. Taday, and A. J. Langley, *J. Phys. B* **33**, 745 (2000).
- [39] D. A. Card, E. S. Wisniewski, D. E. Folmer, and A. W. Castleman, *J. Chem. Phys.* **116**, 3554 (2002).
- [40] W. G. Cochran, *Biometrics* **13**, 261 (1957).
- [41] A. E. Boguslavskiy, J. Mikosch, A. Gijsbertsen, M. Spanner, S. Patchkovskii, N. Gador, M. J. J. Vrakking, and A. Stolow, *Science* **335**, 1336 (2012).
- [42] J. Mikosch and S. Patchkovskii, *J. Mod. Opt.* **60**, 1426 (2013).
- [43] J. Mikosch and S. Patchkovskii, *J. Mod. Opt.* **60**, 1439 (2013).
- [44] C. Madsen, L. Madsen, S. Viftrup, M. Johansson, T. Poulsen, L. Holmegaard, V. Kumarappan, K. Jørgensen, and H. Stapelfeldt, *Phys. Rev. Lett.* **102**, 073007 (2009).
- [45] C. Madsen, L. Madsen, S. Viftrup, M. Johansson, T. Poulsen, L. Holmegaard, V. Kumarappan, K. Jørgensen, and H. Stapelfeldt, *J. Chem. Phys.* **130**, 234310 (2009).
- [46] The MathWorks, Inc., MATLAB 8.0, Natick, MA (2012).
- [47] B. Friedrich and D. Herschbach, *Phys. Rev. Lett.* **74**, 4623 (1995).
- [48] C. S. Slater, Ph.D. thesis, University of Oxford, 2014.